Investigation of the Effects of Transition Reynolds Numbers on Empirical Constants of the Rossiter Formula

Uthpala Kaluwila*, Rho Shin Myong†, Hakjin Lee‡

Gyeongsang National University, Jinju, Gyeongnam, 52828, South Korea

Nomenclature

c = Outside length of the cavity

$\mathbf{C}$ = Collision operator

f_m = Frequency of the mth mode

$\mathbf{F}$ = Probability distribution function of the particles in space and time

K_v = Empirical constant relating the local shear layer velocity and the free stream velocity

L/D = Length to depth ratio of the cavity

m = Mode number

M_∞ = Mach number of freestream

$\mathrm{R_e}$ = Reynolds number

St_m = Strouhal number of the mth mode

Δt = Time step

$\mathbf{V}$ = Particle velocity

α = Empirical constant representing the phase lag of reflected pressure wave

γ = Specific heat ratio of the fluid

τ = Relaxation time

*Graduate Student, School of Mechanical and Aerospace Engineering, AIAA Member
†Professor, School of Mechanical and Aerospace Engineering, Associate Fellow AIAA
‡Assistant Professor, School of Mechanical and Aerospace Engineering, AIAA Member; (Corresponding author: hlee@gnu.ac.kr)

I. Introduction

THE characteristics of the flow field past a cavity are of long-standing research interest in the fields of fluid mechanics and aerodynamics, because cavity structures are essential in a wide range of engineering applications, such as engines, aerodynamic structures, heat exchangers, vehicles, and aircraft. The flow behavior within cavities can have a significant impact on the performance and efficiency of these systems. In addition to unsteady flow physics, the study of cavities includes the analysis of acoustic characteristics. Cavities exhibit complex resonances and standing waves that can produce severe pressure fluctuations and noise [1–3]. This is particularly important in applications where noise levels need to be minimized, such as in aircraft and industrial systems.

The strong interaction between the unsteady flow and cavity structure has implications for both the structural integrity of the cavity and the noise levels. The primary source of this issue arises from periodic fluctuations generated within the cavity. Among these fluctuations, a few specific resonant frequencies have a significant impact [4, 5]. Despite its simple geometry, the mechanism of sound generation within a cavity involves a complex feedback mechanism, in which the shear layer above the cavity hits the rear wall, is reflected, and interacts with the incoming upstream shear layer, creating constructive interference at specific frequencies.

Krishnamurthy [6] first experimentally observed that acoustic tones were produced from a two-dimensional gap, and Rossiter [4] described this phenomenon as a two-dimensional mechanism of tone formation, where the shear layer initiating at the upstream edge gives rise to Kelvin–Helmholtz (KH) vortices. These interact with the downstream edge of the cavity to produce sound, which travels towards the leading edge and gives rise to additional vortices. This results in a feedback loop in which the flow field dynamically interacts with itself. Rossiter proposed a semi-empirical formulation for predicting resonant frequencies ("Rossiter modes") as a function of the flow properties and cavity geometry, which are related to each other by two empirical constants. Heller *et al.* [5] expanded the Rossiter mode formula to include the thermal effects of gas, and applied it to a supersonic flow regime. Plumblee *et al.* [7] introduced another type of mode for rectangular cavities, called the acoustic cavity mode, in which the frequencies can be theoretically predicted for appropriate boundary conditions. Gharib and Roshko [8] experimentally identified another mode of noise generation in a cavity flow, referred to as the wake mode. Rowley *et al.* [9] analyzed the acoustic feedback mechanism and development of KH vortices in shear-layer mixing. They also showed that the length of the cavity affects the level of influence of the wake mode, and that the Rossiter mode affects the noise generated, with longer cavities favoring the wake mode. Brès and Colonius [10] investigated the effect of flow compressibility on the critical Reynolds number, and Sun *et al.* [11]

extended this study to show that at higher Mach numbers, compressibility stabilizes the flow by establishing a neutral curve as a function of the Reynolds and Mach numbers.

Most previous studies have focused on the turbulent region of the cavity flow, adopting both experimental [12–14] and numerical approaches [15, 16]. Few studies have considered the cavity flow at low Reynolds numbers, because such flow conditions are difficult to achieve in a wind tunnel. However, exploring cavity flow at low Reynolds numbers within the transition region can provide valuable insights into the intricate processes of vortex generation and flow interactions occurring within the cavity and shear layer. This is due to the fact that the transition region exhibits significantly more pronounced variations in flow structures, while still retaining essential characteristics of turbulent flow. Although recent efforts have been made to solve such flows computationally and elucidate the underlying physics, most of these have focused on global stability analysis [10, 11, 17, 18]. The Rossiter mode formula was derived from experiments conducted within the turbulent region of Reynolds numbers, including the subsonic and low-supersonic flow regimes. Therefore, this formulation might not be as accurate for flow conditions outside these specific conditions. Moreover, the Rossiter mode formulation consists of two empirical constants: K_v and α. Previous experimental works [1, 18–20] suggested that the exact values of K_v and α, as well as their dependence on the flow conditions and *L/D* ratio, remains an unresolved issue. Therefore, it is reasonable to assume that the empirical constants may be affected by lower Reynolds numbers, particularly within the transitional regime.

The main objective of this study is to investigate the effects of the transitional region of Reynolds numbers on the empirical constants of the Rossiter mode formula. The lattice Boltzmann method (LBM) based commercial software PowerFLOW was used to simulate the flow field of a cavity with an *L/D* ratio of 4.5 at a Mach number of 1.2. LBM simulation to model the turbulence were conducted, and the near-field acoustic spectra were directly resolved using local pressure data for probe locations within the cavity walls. The peak values of the power spectral density (PSD) graphs were used to recalculate the empirical constants of the Rossiter formula. The empirical constants decreased with decreasing Reynolds numbers once the flow crossed the threshold from the fully turbulent region to the transition one.

II. Methodology

A. Rossiter mode formula

The Rossiter mode formula consists of two empirical constants K_v and α, Here, K_v is the empirical constant relating the local shear layer velocity (V_c) and the free stream velocity (V_∞), and α is a constant representing the

phase lag between a vortex hitting the downstream wall and the corresponding pressure wave being reflected upstream. α is a function of the cavity length-to-depth (*L/D*) ratio. The original Rossiter's formulation is given in Eq. (1), where St_m is the Strouhal number representing the non-dimensionalized frequency with respect to cavity length. Here, *m* denotes the number of modes.

$$St_m = \frac{f_m}{L} = \frac{m - \alpha}{M_\infty + \frac{1}{k_v}} \tag{1}$$

The original Rossiter's formulation was amended by Heller [21] to include the thermal effects, which can be rearranged in Eq. (2) to be able to calculate the empirical constants through a linear data fit of the obtained Rossiter resonant frequency values.

$$St_m = \frac{f_m}{L} = \frac{m}{\frac{M_\infty}{\sqrt{1+\frac{\gamma-1}{2}M_\infty^2}} + \frac{1}{K_v}} - \frac{\alpha}{\frac{M_\infty}{\sqrt{1+\frac{\gamma-1}{2}M_\infty^2}} + \frac{1}{K_v}} \tag{2}$$

Acoustic data in the time domain were directly obtained from the flow analysis of the cavity via LBM simulations. Because the LBM used in this study is intrinsically compressible and unsteady, it is ideal for directly resolving the acoustic field using pressure fluctuations [22]. Variations in acoustic pressure in the time domain (obtained at probe locations on the cavity floor, as shown in Fig. 1) were transformed into the frequency domain via a fast Fourier transformation to obtain the acoustic spectrum. The values of K_v and α can be derived using the Strouhal numbers corresponding to the peak PSD identified in the simulation results.

B. Lattice Boltzmann method

The governing equation for the LBM is the lattice Boltzmann equation, which is a time-dependent equation expressing the Boltzmann equation in a simplified form; it represents the behavior of a fluid in terms of its velocity distribution functions. In the LBM, the Boltzmann equation is discretized on a lattice, resulting in a set of discrete equations that describe the evolution of probability distribution functions (PDFs); this ensures efficient and scalable simulations [23]. The PDFs are discretized in the velocity space, and the collisions between particles are modeled using a collision operator. The distribution functions are the primary variables in the LBM simulation, and they evolve over time owing to the interactions between particles.

The movement of a flow particle can be defined by advection or collision, and its governing equation is expressed as follows:

$$\frac{\delta \mathbf{F}}{\delta t} + \mathbf{V} \cdot \nabla \mathbf{F} = \mathbf{C} \tag{3}$$

where **F** is the probability distribution function of the particles in space and time, **V** is the particle velocity, and **C** is the collision operator. Eq. (4) can be discretized in space (**x**) and time (t), as shown in Eqs. (4) and (5).

$$\mathbf{F}_n(\mathbf{x} + \mathbf{V}_n \Delta t,\ t + \Delta t) - \mathbf{F}_n(\mathbf{x}, t) = \mathbf{C}_n(\mathbf{x}, t) \tag{4}$$

$$\mathbf{C}_n = \frac{\Delta t}{\tau}[\mathbf{F}_n(\mathbf{x}, t) - \mathbf{F}_n^{eq}(\mathbf{x}, t)] \tag{5}$$

$$\tau_{eff} = \tau = C_\mu \frac{k^2/\varepsilon}{\sqrt{1 + \eta^{-2}}} \tag{6}$$

The discretized equation is solved in a lattice using a Cartesian reference system. Here, $\mathbf{F}_n$ and $\mathbf{V}_n$ are the distribution function in the n-th direction and the discretized velocity factor of a particle relative to the lattice orientation, respectively. The Bhatnagar–Gross–Krook (BGK) model [24] is used to express the collision term $\mathbf{C}_n$, with τ and $\mathbf{F}_n^{eq}$ being the relaxation time and equilibrium Maxwell–Boltzmann distribution function, respectively. Lattice Boltzmann method-very large eddy simulation. Interpreting the lattice Boltzmann equation is equivalent to directly simulating the Navier-Stokes equation within the dynamic range (Mach number) of the number of discrete particles and the limits of lattice resolution, to capture the smallest magnitude of turbulence. In this study, a modified form of the renormalization group (RNG) k-ε model was applied to the LBM for turbulence modeling; this is called the LBM-very large eddy simulation (LBM-VLES) [25], which is conceptually equivalent to hybrid methods such as detached eddy simulation. An eddy viscosity term is included in the collision term $\mathbf{C}_n$ of Eq. (5) [26], and this equation modifies the relaxation properties, facilitating the development of large eddies in the flow field. The RNG k-ε model is used to calculate the turbulence relaxation time, which is added to the viscous relaxation time, as defined in Eq. (6). Here, $C_\mu = 0.09$ and η are a function of the turbulent kinetic energy.

III.Computational setup

A. Cavity model and computational grid

A three-dimensional model of a cavity with an L/D of 4.5 was used for all simulation cases, as shown in Fig. 1. The cavity was modeled using the dimensions of the cavity model in the experiments conducted by Dix and Bauer [27] and Suh [28]. An outside cavity length (C) of 47 inches was used as the characteristic length to determine the size of the computational domain. The cavity was situated in a box-shaped flow domain with each side located 50 times the outside cavity length away from the origin, as shown in Fig. 2. The computational domain

was spatially discretized into Cartesian meshes called voxels. Local mesh refinement in the computational domain can be controlled using defined variable refinement (VR) regions, where the refinement of two adjacent VR regions can vary by a volume factor of four. A velocity inlet boundary condition was imposed on the inlet side of the computational domain, whereas a static pressure outlet boundary condition was applied at the far-downstream end. A velocity boundary condition was imposed on the remaining four far-field sides.

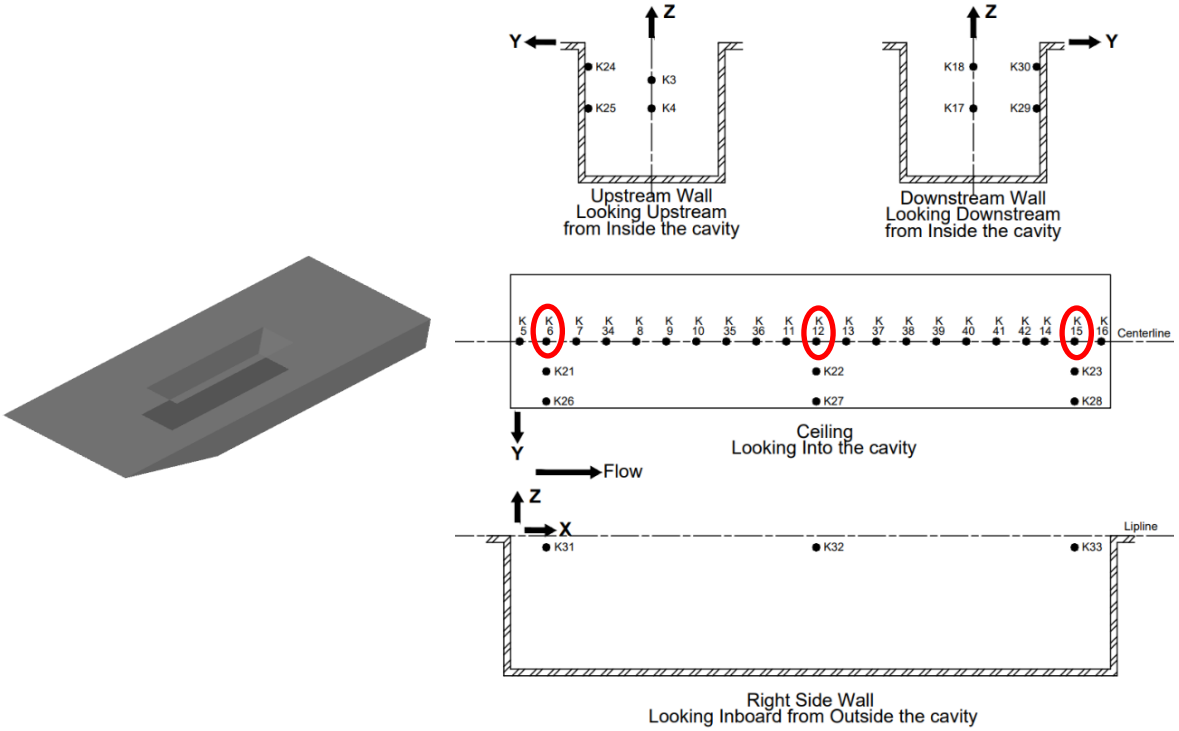

Fig. 1 Three-dimensional model of the cavity and acoustic probe locations
(Probe locations used in the following sections of the paper circled)

B. Grid dependency test and validation

Prior to investigations of the Rossiter modes within the transitional flow regime of Reynolds numbers, the computational setup was validated and compared against the results of a wind tunnel experiment conducted at the United States Air Force Arnold Engineering Development Center [27, 28]. A Mach number of 1.2 was used for validation in this study, and the detailed flow conditions are listed in Table 1. A grid-dependency test was performed for three different grid resolutions, to assess the effect of the mesh quality on the acoustic results. The details of the three grid systems are presented in Table 2. The three meshes were similar in all aspects except for the resolution of the volume grid. The elapsed simulation time for an Intel Xeon SPG-6230R 2.1 GHz processor with 52 cores was compared for each grid resolution, without considering any setup time of for the preprocessor

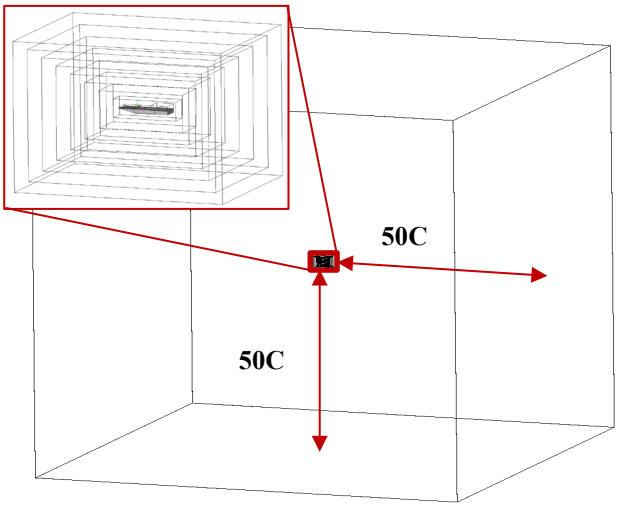

Fig. 2 Computational domain for simulating three-dimensional cavity

Table 1 Flow conditions for LBM solver validation

Mach number	Pressure (psf)	Temperature (°R)	Reynolds number
1.2	1200	550	1.9×10^6

Table 2 Grid systems for dependency testing

Parameter	Low quality	Medium quality	High quality
VR resolution	25	50	100
Smallest voxel size	0.0041 m	0.0020 m	0.0010 m
Total number of voxels	2,042,009	14,716,423	100,167,581
Simulation time	2.647 hours	22.52 hours	258.2 hours

Figure 3 compares the time-averaged coefficient of pressure along the streamwise centerline floor of the cavity. The numerical results obtained from LBM simulations with three different grid system resolutions were compared with the experimental data. This indicates that the results of the pressure coefficient fall well within the range of the experimental results and do not exhibit a considerable difference between the medium- and fine-mesh qualities. However, a slight discrepancy was found between the results of the coarse grid and the measurements, especially at the forward end of the cavity.

The acoustic spectra obtained for the different cavity probes along the cavity floor centerline are compared in Fig. 4. The probes were placed within the cavity geometry to record the pressure data required for acoustic analysis. These locations exactly matched the pressure transducer locations used in the experiments [27, 28], as shown in Fig. 1. The acoustic results aligned exceptionally well with the experimental results for both medium and fine

meshes. However, whilst the resonant peak frequencies matched well with the measurements in the coarse mesh, the amplitudes of the peaks in the low-frequency range appear to be overpredicted at the peaks and underestimated in the broadband region. The experimental results show an increase in broadband noise at around 3,000–4,000 Hz (Strouhal numbers 4–5), which was attributed to the wind tunnel background noise in the original work [27]. The resonant frequencies and amplitudes were captured accurately at both medium and fine grid resolutions. Because no significant difference was observed in the quality of the results between the medium and fine mesh resolutions, the medium-quality mesh was used in all subsequent simulations, owing to its superior time efficiency. The resonant frequencies obtained from the Rossiter equation, experiments, and LBM simulations are listed in Table 3. Regardless of the location, the resonant frequencies exactly matched the experimental results. The Rossiter equation predictions were very close to the experimental results; hence, it can be stated that the empirical constants are sufficiently accurate for the turbulent Reynolds number range.

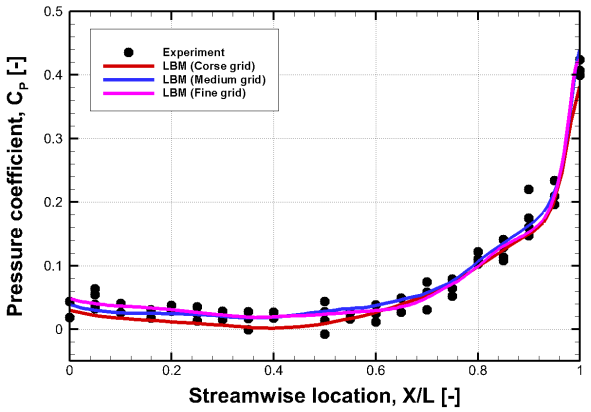

Fig. 3 Pressure coefficients along the streamwise centerline floor of the cavity

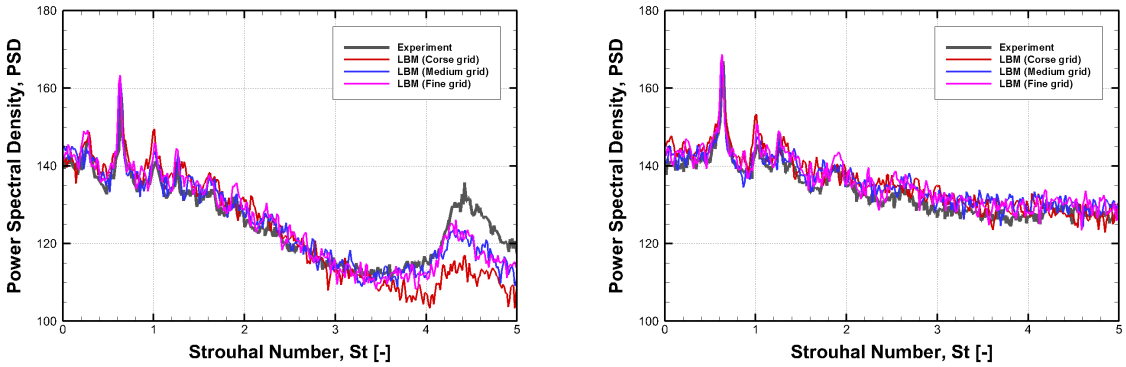

(a) K6 probe

(b) K12 probe

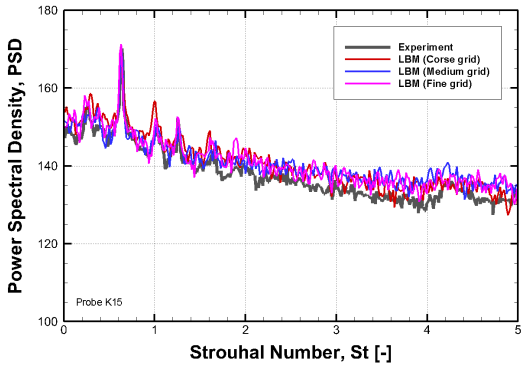

(c) K15 probe

Fig. 4 Acoustic spectra of different cavity probes along the cavity floor centerline

Table 3 Resonant frequencies obtained from experiments, Rossiter equation, and LBM simulation

Mode	Experiment	Rossiter equation	Present (medium mesh)
1	0.253	0.249	0.258
2	0.629	0.595	0.632
3	1.101	0.941	1.000
4	1.261	1.287	1.265

IV. Results and discussion

A. Flow conditions

LBM simulations of unsteady flow over a three-dimensional cavity model with an *L/D* ratio of 4.5 were conducted to investigate the effects of the transition Reynolds numbers on the cavity flow and its resonant frequencies. The simulated flow conditions were adjusted by changing the pressure whilst maintaining a constant Mach number and ambient temperature. The ambient temperature was fixed at 270.65 K, and a velocity of 396 m/s was used (which corresponds to a Mach number of 1.2). The Reynolds number was defined with respect to the cavity depth as Re_D, and a summary of the flow conditions for each case is listed in Table 4.

Table 4 Flow conditions

Reynolds number (Re_D)	**2282**	**3004**	**4005**	**6008**	**8000**	**10013**	**12017**	**14018**	**16003**
Pressure (Pa)	75.9	105	140	210	279.6	350	420	504	559.3

B. Effect of a transitional Reynolds number on the cavity flow characteristics

Prior to investigating the effect of the transitional Reynolds number on the cavity acoustics, the flow characteristics inside the cavity were analyzed for various Reynolds numbers. Fig. 5 shows the averaged streamlines of the three selected cases within the transition region and the fully turbulent case used in the validation. The recirculation region can be clearly observed in all cases along with the evolution of the vortex structures across the Reynolds numbers. As expected, the incoming flow hit the rear wall and was redirected inside the cavity. The internal coherent structures seemed to primarily consist of two structures: a circulation region at the rear end that redirected the flow towards the front of the cavity and a helically shaped vortex moving from the front of the cavity and cutting through the aforementioned structure to rejoin the main flow out of the cavity. At lower Reynolds numbers, the circulation region was more dominant, and the helical vortex was restricted to a very small region at the top layer of the flow. Whilst the velocities within the circulation region increase as the flow becomes increasingly turbulent, the structural dimensions seem to be largely unaffected. This is unlike the helical structure, which seems to develop rapidly with increasing Re, becoming a dominant structure by the time the flow becomes fully turbulent. This observation falls well within the observed amplitude increase under increasing Reynolds number, because a more violent interaction between coherent vortex structures produces an increased output of the acoustic amplitude.

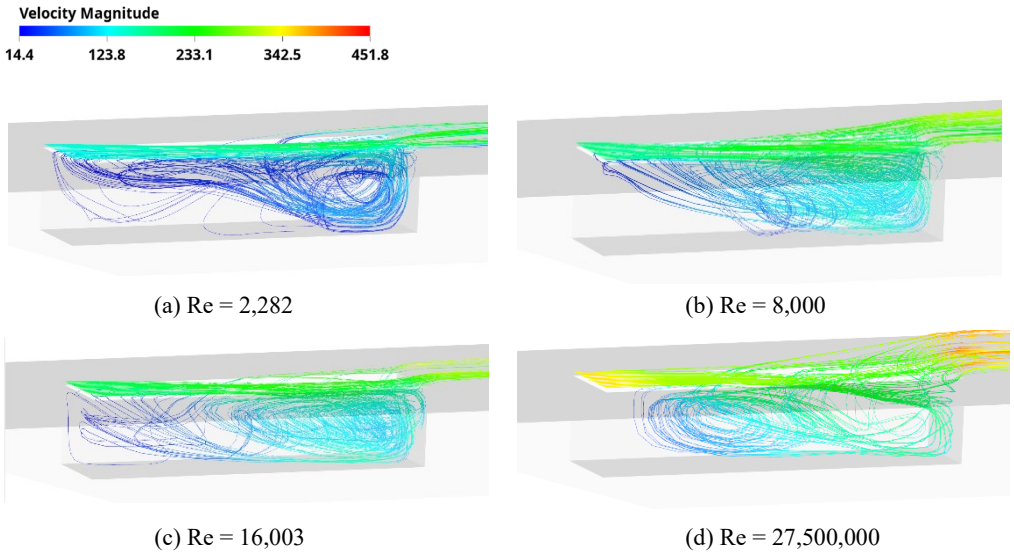

(a) Re = 2,282 (b) Re = 8,000

(c) Re = 16,003 (d) Re = 27,500,000

Fig. 5 Averaged flow streamlines inside the cavity at different Reynolds numbers

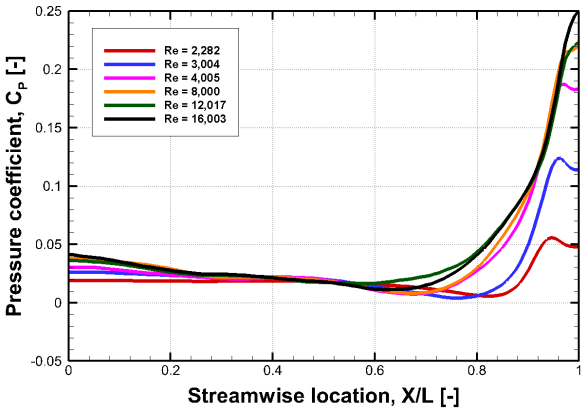

Fig. 6 Time-averaged pressure coefficient along centerline of cavity floor

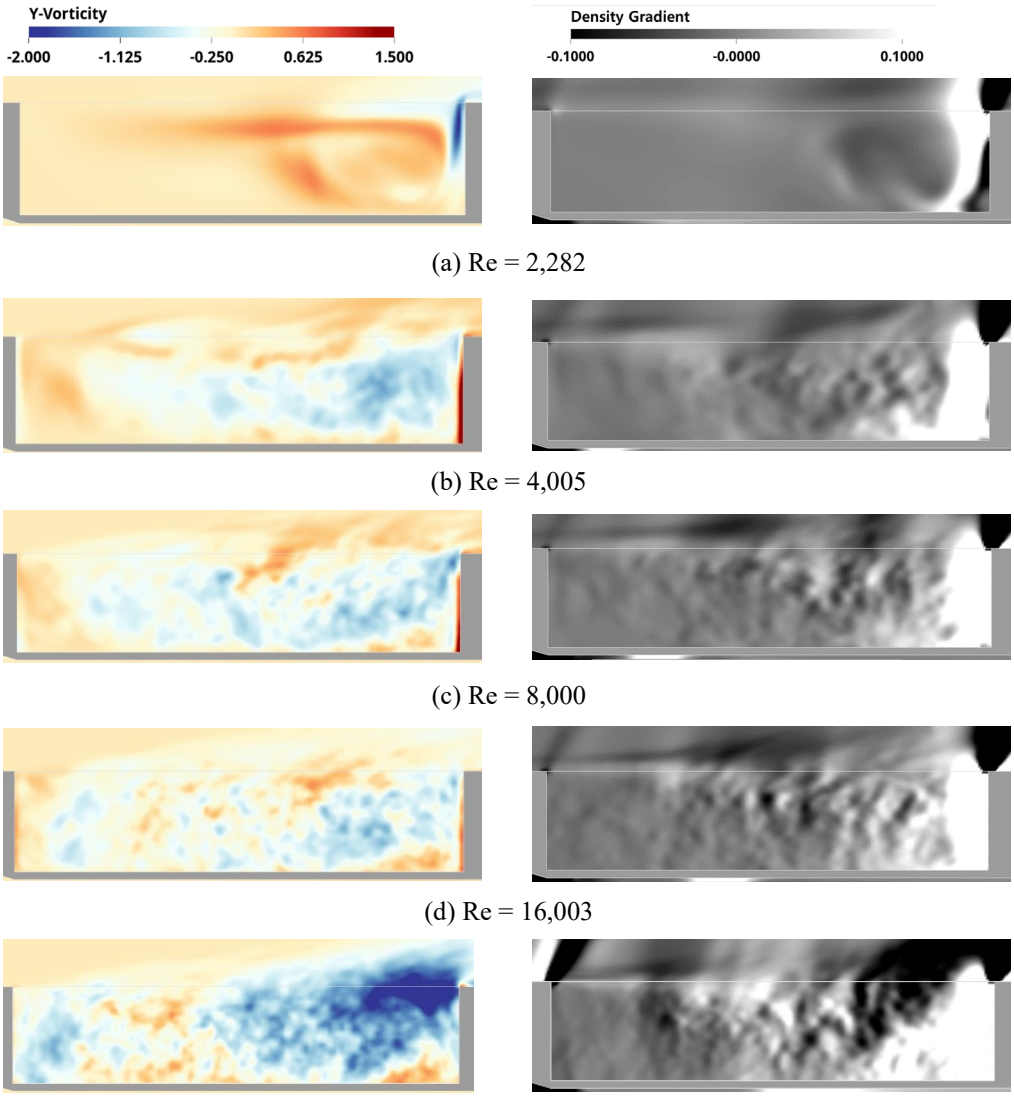

(a) Re = 2,282

(b) Re = 4,005

(c) Re = 8,000

(d) Re = 16,003

(e) Re = 1.9×10^6 (Validation case)

Fig. 7 Instantaneous vorticity (left) and x-direction density gradient (right) along centerline for different Reynolds numbers

Figure 6 shows the time-averaged coefficient of pressure for different Reynolds numbers along the centerline floor. The coefficient of pressure did not differ significantly at the front edge of the cavity, where the effect of the shear layer was minimal; however, it did affect the rear end of the cavity more prominently. The variation in C_P correlates with the vortex structures shown in the averaged streamline contour, where different vortical structures shift in size and location with respect to the Reynolds number. The rearmost edge at the cavity floor seems largely untouched by the vortex above it at lower Reynolds numbers, resulting in a dip in the C_P contour at the point where the vortex detaches from the floor.

Figure 7 presents the instantaneous vorticity and density gradient fields. The flow was very smooth with only one distinct eddy structure in the case of Re = 2,282, and the vortex structures became increasingly chaotic as the Reynolds number increased. The effect of the shear layer interaction continued to advance upstream under the increase in Reynolds number. The kinetic energy of the flow hitting the rear wall increased with the Reynolds number, allowing the redirected particles to travel further upstream before losing their backward momentum and rejoining the downstream flow. The vorticity structures seemed to reach the forward wall of the cavity by Re = 16,003; furthermore, they appeared to exhibit a similar layout to the fully turbulent vorticity field in the fully turbulent case, Fig. 7(e), albeit with a much lower intensity.

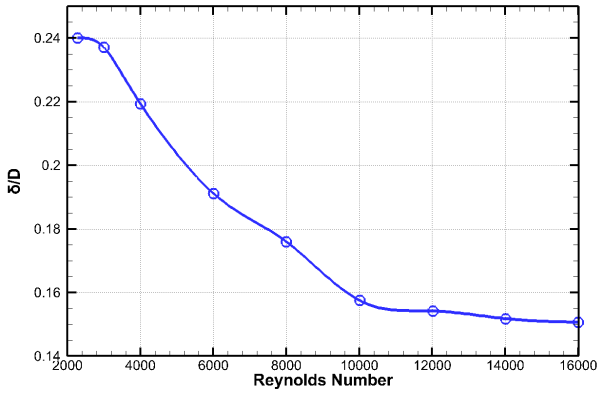

Fig. 8 Measured boundary layer thickness at different Reynolds number

The thickness of incoming boundary layer, which is one of the important parameters for Rossiter modes, at the center of the forward edge of the cavity was measured and the non-dimentionalized values were plotted against the Reynolds numbers as shown in Fig. 8. It can be seen that the boundary layer thickness reduces with increasing Reynolds numbers in a relationship not unlike that of a flat plate, and the incoming boundary layer start to converge to a value around 0.15 around the vicinity of Reynolds 12,000.

C. Effect of a transitional Reynolds number on the Rossiter mode formula

Figure 9 shows the power spectral density contours of all simulated Reynolds numbers: the overall amplitudes reduced whilst the peak frequencies shifted leftwards under reducing Reynolds numbers. Both these changes become more drastic at lower Reynolds numbers. Because these structures are the source of acoustic generation within the cavity, this change is also reflected in the flow streamline profiles shown in Fig. 5 and Fig. 7, where the intensity of the vorticity increases under an increasing Reynolds number. The shift in the flow vortices was much more drastic at lower Reynolds numbers, whereas a few dominant vortices stabilized under increasing turbulence. Because these dominant structures do not shift further once the flow is fully turbulent, the resonant frequencies do not shift (despite the overall amplitude increase), as observed by both Heller and Rossiter. Whilst the overall amplitudes of the graphs increased, the contrast between the peaks and valleys decreased as the Reynolds number increased, and only a few resonant peaks appeared to emerge from the existing broadband spectra. For the Reynolds numbers above 10,000, only four clear peaks were observed, and for all Reynolds numbers below we see five discernible peaks, except for the final case of Re = 2,282, where many more nodes can be observed and where even-numbered modes dominate over odd-numbered ones. This indicates that broadband noise has a much greater effect on the overall noise profile at higher flow turbulence and overpowers the resonant noise amplitudes much more easily at higher frequencies.

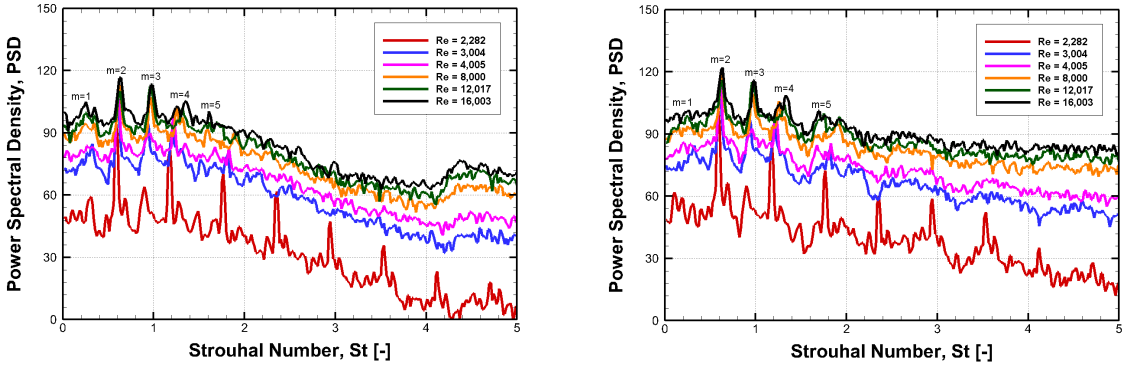

(a) K6 probe

(b) K12 probe

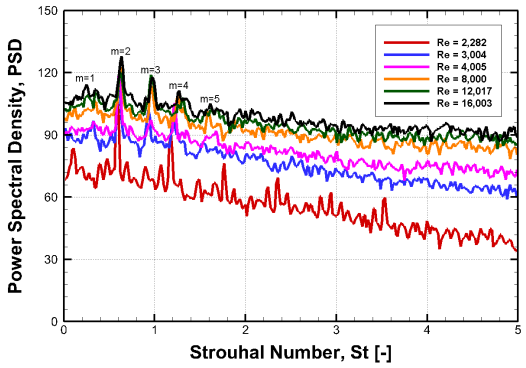

(c) K15 probe

Fig. 9 Acoustic spectra for all investigated Reynolds numbers

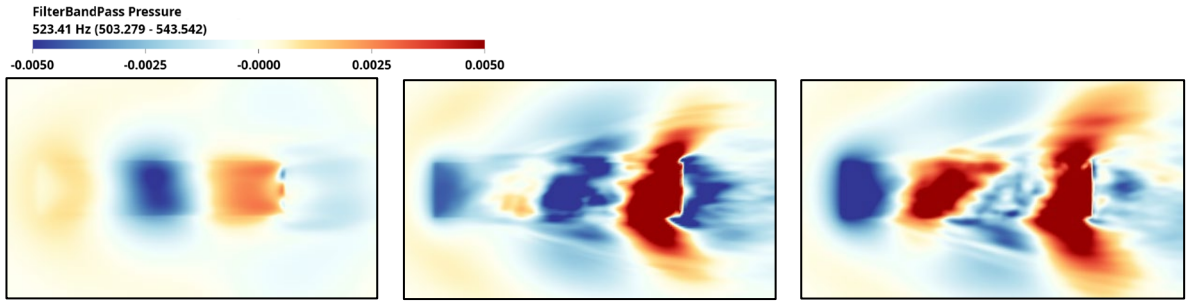

(a) Re = 2,282 (b) Re = 8,000 (c) Re = 16,003

Fig. 10 Dilation field on the plane of the cavity lipline

Figure 10 presents the pressure dilation field on the plane of the cavity lip (refer to Fig. 1 for the lip line location) with the band filtered between the frequency ranges of 500 and 600 Hz. As shown in Fig. 9, mode 2 (m = 2) is the dominant resonant mode, and a frequency range encompassing the resonant mode 2 (m = 2) was selected for the band pass filter analysis. At very low Reynolds numbers, the cavity seems to resonate very stably with clear lobes, which could explain the relatively large contrast between the peaks and valleys in the PSD contour, as shown in Fig. 9 for Re = 2,282. When the Reynolds number increases, the resonant lobes become much less geometrically coherent and increase in intensity; this is also reflected in the PSD contour as a decreasing contrast between the valleys and peaks and an increase in the Reynolds number.

Only the acoustic data obtained from the position of probe K6 were used for a detailed analysis of the acoustic properties of the cavity in the transition flow region, because this probe location matched the experimental data most accurately whilst also showing comparatively more distinguished resonant peaks for a greater number of Rossiter modes before fading. The peak values were obtained from the PSD graphs, and the values of K_v and α were calculated using the Rossiter equation in the form of Eq. (2). The variation of the values of K_v and α are shown in Table 5 and depicted in Fig. 11 for the different Reynolds numbers. The values of K_v and α approached the Rossiter values as the flow became more turbulent, fully reaching the values 0.57 and 0.28, respectively, at a Reynolds number of 12,000; this supports the claim made by both Rossiter and Heller: that for a sufficiently turbulent flow, the resonant frequencies are independent of the Reynolds number. However, it is apparent that these constant values are only relative to a flow condition in which the flow is sufficiently turbulent and changes in the Reynolds number do not significantly affect the vortex structure of the flow within the cavity. Prior to this,

the vortex structures are very sensitive to changes in the Reynolds number and by extension, as are the resonant peaks of the acoustic spectra. When compared to the incoming boundary layer thickness graph in Fig. 8, it can be seen that the point at which the empirical constants approach the Rossiter's values corresponds to the Reynolds number where the boundary layer thickness is also starting to converge, showing that there is an intrinsic relationship between the two parameters. As mentioned previously, the vortical structures do not encompass the entire cavity structure until a relatively high Reynolds number (Re ≈ 12,000). As shown in Fig. 7, the vortical structure does not affect the front edge of the cavity at lower Reynolds numbers. It can be concluded that this leads to the flow developing smaller recirculation regions, resulting in lower resonating frequencies. Once the Reynolds number increases sufficiently for the recirculation region to reach the front wall, the cavity structure itself restricts further increases in size, causing the resonant frequency to remain unchanged under further increases in Reynolds number. This makes the values of the two constants dependent on the Reynolds number under increasing K_v and α, with increasing Reynolds numbers showing that, within the transition region, the values of the empirical constants need to be adjusted for the Rossiter predictions to be accurate.

Table 5 Calculated values of empirical constants

Reynolds number (Re_D)	a	b	K_v	α
2282	0.2913	0.0154	0.421	0.0529
3002	0.2975	0.0231	0.434	0.0776
4003	0.3192	0.0311	0.482	0.0974
6005	0.3347	0.0544	0.518	0.1625
8000	0.3332	0.0636	0.514	0.1909
10013	0.3518	0.0853	0.560	0.2425
12017	0.3564	0.1009	0.572	0.2831
14018	0.3595	0.1009	0.580	0.2807
16003	0.3584	0.097	0.577	0.2706

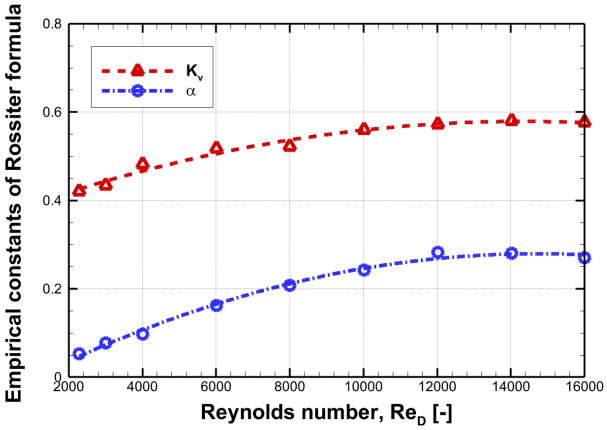

Fig. 11 New empirical constants calculated from LBM simulation results

V.Conclusion

In this study, the aerodynamic and acoustic characteristics of the flow past a cavity with an *L/D* of 4.5 under different Reynolds numbers including the transition regime were investigated using LBM–VLES simulations. The near-field acoustic spectra were directly resolved using the local pressure data for the probe locations within the cavity walls. Eight cases were simulated within the Reynolds number range of 2,000–16,000. The amplitude of the PSD decreased under decreasing Reynolds number. Although the resonant frequencies remained within a tight range, a slight shift of the peaks to the left (decreasing) was observed under decreasing Reynolds numbers, indicating that the Rossiter predictions were inaccurate at the Reynolds numbers for the transitional region. The peak values of the graphs were used to back-calculate the empirical constants (K_v and α) of the Rossiter formula; they showed that both K_v and α increased with increasing Reynolds number and settled at Rossiter's proposed values of 0.57 and 0.28, respectively, when the flow became turbulent. It can be concluded that whilst the original Rossiter formulation still holds true, it should be adjusted if it is to be used over a range of transitional Reynolds numbers. The empirical constants are the asymptotic end values at which the flow becomes fully turbulent. This study will be extended to include different *L/D* ratios and different Mach numbers, to obtain a full picture of the variation in the values (K_v and α), such that an accurate relationship can be formulated to predict the resonant frequencies at these Reynolds numbers and fully elucidate the underlying flow physics.

This study is the initial step intended as the starting point to investigate the empirical values of the Rossiter formulation for the transitional Reynolds numbers. The objective of the current study was to confirm the initial hypothesis of empirical constants of the Rossiter formula are not constant within the transition region. Therefore, the number of datapoints obtained in the current study is not adequate to form and an accurate regression formula which would accurately encompass the transitional region as this study only looked at a few Reynolds numbers for a single Mach number and cavity L/D ratio. Further simulations covering a range of Mach numbers, Reynolds numbers and cavity geometries will be carried out to attempt to develop a proper relationship between Reynolds number and empirical constants of the Rossiter Formula within the transitional region.

Acknowledgments

This study was supported by the National Research Foundation of Korea (NRF) grant funded by the Ministry of Science and ICT (NRF-2017-R1A5A1015311 and NRF-2021R1C1C1010198).

Declaration of competing for interest

The authors declare that they have no known competing financial interests or personal relationships that could have appeared to influence the work reported in this paper.

References

1. Unalmis OH, Clemens NT, Dolling DS (2004) Cavity Oscillation Mechanisms in High-Speed Flows. AIAA J 42:2035–2041. https://doi.org/10.2514/1.1000
2. Yamouni S, Sipp D, Jacquin L (2013) Interaction between feedback aeroacoustic and acoustic resonance mechanisms in a cavity flow: A global stability analysis. J Fluid Mech 717:134–165. https://doi.org/10.1017/jfm.2012.563
3. Howe MS (2004) Mechanism of sound generation by low Mach number flow over a wall cavity. J Sound Vib 273:103–123. https://doi.org/10.1016/S0022-460X(03)00644-8
4. Rossiter J (1966) Wind-tunnel experiments on the flow over rectangular cavities at subsonic and transonic speeds. London
5. Heller HH, Holmes DG, Covert EE (1971) Flow-induced pressure oscillations in shallow cavities. J Sound Vib 18:545–553. https://doi.org/10.1016/0022-460X(71)90105-2
6. Krishnamurty K (1956) Acoustic Radiation from Two-dimensional Rectangular Cutouts in Aerodynamic Surfaces. Washington
7. Plumblee HE, Gibson JS, Lassiter L. (1962) Theoretical and Experimental Investigation of The Acoustic Response of Cavities in an Aerodynamic Flow
8. Gharib M, Roshko A (1987) The effect of flow oscillations on cavity drag. J Fluid Mech 177:501–530. https://doi.org/10.1017/S002211208700106X
9. Rowley CW, Colonius T, Basu AJ (1999) Computation of sound generation and flow/acoustic instabilities in the flow past an open cavity
10. Brés GA, Colonius T (2008) Three-dimensional instabilities in compressible flow over open cavities. J Fluid Mech 599:309–339. https://doi.org/10.1017/S0022112007009925
11. Sun Y, Taira K, Cattafesta LN, Ukeiley LS (2017) Biglobal instabilities of compressible open-cavity flows. J Fluid Mech 826:270–301. https://doi.org/DOI: 10.1017/jfm.2017.416
12. Thangamani V (2019) Mode Behavior in Supersonic Cavity Flows. AIAA J 57:3410–3421.

https://doi.org/10.2514/1.J057818

13. Sarohia V (1977) Experimental Investigation of Oscillations in Flows Over Shallow Cavities. AIAA J 15:984–991. https://doi.org/10.2514/3.60739
14. Daoud M, Naguib AM, Bassioni I, et al (2006) Microphone-Array Measurements of the Floor Pressure in a Low-Speed Cavity Flow. AIAA J 44:2018–2023. https://doi.org/10.2514/1.18129
15. Koch W (2005) Acoustic Resonances in Rectangular Open Cavities. AIAA J 43:2342–2349. https://doi.org/10.2514/1.10975
16. Woodruff S (2010) Coupled RANS/LES for SOFIA Cavity Acoustic Prediction. In: 48th AIAA Aerospace Sciences Meeting Including the New Horizons Forum and Aerospace Exposition. American Institute of Aeronautics and Astronautics, Reston, Virigina
17. Schmit RF, Grove JE, Semmelmayer F, Haverkamp M (2014) Nonlinear Feedback Mechanisms Inside a Rectangular Cavity. AIAA J 52:2127–2142. https://doi.org/10.2514/1.J052804
18. Mathias MS, Medeiros MAF (2021) The effect of incoming boundary layer thickness and Mach number on linear and nonlinear Rossiter modes in open cavity flows. Theor Comput Fluid Dyn 35:495–513. https://doi.org/10.1007/s00162-021-00570-2
19. Zhang X, Edwards JA (1990) An investigation of supersonic oscillatory cavity flows driven by thick shear layers. Aeronaut J 94:355–364. https://doi.org/DOI: 10.1017/S0001924000023319
20. Maciulaitis A (1980) Improved Prediction of Frequency Modes for Peak Amplitude Pressures in Simulated Bomb Bays at Mach 0.6 to 3.0. Memo RM-708
21. Heller HH, Holmes DG, Coert EE (1971) Flow-induced pressure oscillations in shallow cavities. J Sound Vib 18:545–553
22. Brionnaud R, Trapani G, Chávez Modena M, Holmanx DM (2016) Direct noise computation with a lattice-boltzmann method and application to industrial test cases. In: 22nd AIAA/CEAS Aeroacoustics Conference, 2016. pp 1–20
23. Chen S, Doolen GD (1998) Lattice Boltzmann Method for Fluid Flows. Annu Rev Fluid Mech 5:9507
24. Bhatnagar PL, Gross EP, Krook M (1954) A model for collision processes in gases. I. Small amplitude processes in charged and neutral one-component systems. Phys Rev 94:511–525. https://doi.org/10.1103/PhysRev.94.511
25. Chen H, Teixeira C, Molvig K (1998) Realization of fluid boundary conditions via discrete boltzmann dynamics. Int J Mod Phys C 9:1281–1292. https://doi.org/10.1142/S0129183198001151

26. Teixeira CM (1998) Incorporating Turbulence Models into the Lattice-Boltzmann Method. Int J Mod Phys C 09:1159–1175. https://doi.org/10.1142/S0129183198001060

27. Dix RE, Bauer RC (2000) Experimental and Theoretical Study of Cavity Acoustics AEDC-TR-99-4

28. Suhs NE (1992) Transonic Flow Calculations for a Cavity with and without a Store AEDC-TR-92-4. TENNESSEE